2023 IEEE International Conference on Robotics and Automation (ICRA 2023)
May 29 - June 2, 2023. London, UK

A Kinematically Redundant (6+1)-dof Hybrid Parallel Robot for Delicate Physical Environment and Robot Interaction (pERI)

Jehyeok Kim and Clément Gosselin, *Fellow, IEEE*

***Abstract*— A novel kinematically redundant 6+1-degree-of-freedom (dof) spatial hybrid parallel robot is proposed. Each of the two legs of the robot has a fully parallel structure to minimize the moving inertia by mounting actuators on the base. The kinematic model of each leg and overall robot architecture is developed based on the constraint conditions of the robot geometry. The singularity analysis of legs 1 and 2 reveals that their serial and parallel singularities can be avoided by properly dimensioning the robot and sacrificing the edge of the workspace. In addition, it is shown that the type II (parallel) singularities can be completely avoided, resulting in a large orientational workspace. The gripping mechanism is then introduced which is operated by the redundant degree of freedom of the robot. A CAD model of the robot and a computer animation are provided to demonstrate the positioning and orientation of the robot and the gripping function.**

I. INTRODUCTION

Manipulation robots capable of delicate physical interaction (PI) are essential for automating physical contact-sensitive tasks, such as electronics assembly. Previous manipulation robots combined with a vice-type gripper have been successfully applied to pick-and-place tasks where payloads are relatively heavy and the significance of contact conditions is low [1]–[3]. However, due to the large moving inertia and high impedance of the manipulation robots, this approach is not appropriate for tasks in which the objects handled are relatively light and vulnerable to collisions. For the delicate PI, the robot should achieve spatial manipulation with low moving inertia, low impedance, and high precision simultaneously.

As an approach that can reduce the moving inertia, several studies proposed in-hand manipulation that changes the local position and orientation of an object by multi-degree-of-freedom grippers [4]–[10]. These grippers can obtain low moving inertia owing to the light weight of the fingers. Nevertheless, since the in-hand manipulation is generated under independent motion between the gripper and the object, it is difficult to guarantee high precision. Several researchers attempted to develop grippers with low impedance using direct-drive actuation [11]–[14]. Even though these grippers achieved low impedance and low moving inertia, they only produce a planar grip motion. Y. Karako et al. proposed a gripper actuated by eight direct-drive motors. The gripper can generate spatial local manipulation of the object with low impedance [14]. However, since the object and the fingers are connected by contact, the kinematic model varies according to the contact condition changes, resulting in unstable precision.

Parallel architectures constitute promising alternatives as manipulation robots that achieve the required performance for delicate PI. Parallel robots are advantageous for lowering the moving inertia since the actuators can be fixed to the base. In addition, because gravitational torques generated by the robot's weight are significantly low, it is possible to greatly reduce the impedance of parallel robots by utilizing direct-drive actuation. A disadvantage of parallel robots is a limited orientational workspace due to type II singularities. In order to alleviate this drawback, several studies proposed kinematically redundant (KR) architectures that can be used to avoid such singularities, without introducing actuation redundancy. In [15], [16], the authors proved that a KR (3+3)-dof mechanism can avoid all type II singularities. Spatial KR architectures with the same capability of singularity avoidance were suggested in [17], [18]. Although KR parallel robots have advantages for the PI, there is a limit to lowering the moving inertia because an additional gripper must be attached to a moving platform of the robot.

Recently, several studies presented KR parallel or hybrid architectures with an integrated gripper. In [19] and [20], [21], the authors presented a (3+1)-dof parallel mechanism for planar manipulation and a (6+3)-dof hybrid parallel mechanism for spatial manipulation, respectively. The (6+3)-dof mechanism achieved low impedance through the direct-drive actuation. Moreover, since there is no change in contact conditions between a gripped object and the robot during positioning and orientation, stable precision can be secured. It is noteworthy that the proposed mechanisms utilize kinematic redundancy to not only completely avoid the type II singularities but also implement a gripping function. Because these robots do not require independent grippers, low moving inertia can be achieved. Therefore, this approach is attractive for delicate PI. However, the (3+1)-dof mechanism cannot be applied to spatial manipulation. For the (6+3)-dof mechanism, the number of limbs and actuators, and the existence of floating actuators hinder the maximization of the workspace and minimization of the moving inertia.

In this study, we propose a (6+1)-dof kinematically redundant parallel robot to overcome the limitations of the (6+3)-dof mechanism. The robot architecture has all the advantages required for delicate manipulation since the same principle as the one used in [21] is applied. One redundant dof is used effectively to not only avoid the parallel singularities but also generate a gripping function. This robot has two legs

*The financial support of the Natural Sciences and Engineering Research Council of Canada (NSERC) is gratefully acknowledged.

The authors are with the Department of Mechanical Engineering, Université Laval, Québec, Qc, Canada, jehyeok.kim.1@ulaval.ca, gosselin@gmc.ulaval.ca

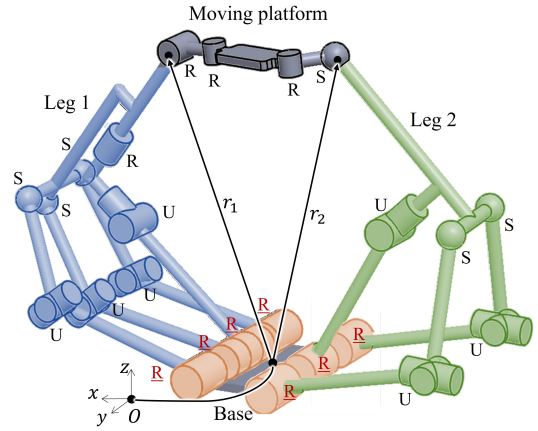

Fig. 1. Architecture of the proposed hybrid parallel robot.

that generate 3-dof and 4-dof respectively and 7 actuators. The reduction of the number of legs and actuators enables a lighter and more compact design. Moreover, to minimize the moving inertia by attaching the actuators at the base, the legs are designed as fully parallel architectures respectively described as RU/2-RUS and RUR/3-RUS, where R stands for a revolute joint, S stands for a spherical joint and U stands for a universal joints, with underlined joints actuated.

This paper is structured as follows. Section II explains the architecture of the proposed robot. The development of the kinematic model is presented in Section III. In Section IV, the type I and II singularities of the architecture are analyzed in detail. Section V explains the gripper mechanism operated by the kinematic redundancy. Finally, Section VI illustrates the global design of the robot and presents computer animations.

II. Robot Architecture

The proposed robot architecture consists of two different legs connecting a moving platform to the base, as illustrated in Fig. 1. The first leg (or leg 1) has one RUR and three identical RUS chains, which can be described as RUR/3-RUS. The first actuated R joints of each chain are mounted on the base in a coaxial configuration to allow a compact footprint and large workspace. In the RUR chain, the axes of the U joint are respectively parallel and perpendicular to the axis of the actuated R joint and to the axis of the last R joint. The end link of leg 1 is connected to this last R joint. In the RUS chains, the first axis of the U joint is parallel to the axis of the R joint. Each RUS chain is connected to the end link by a spherical joint. As a result, leg 1, with four actuated revolute joints, can generate four dofs, namely three dofs for positioning and one dof of rotation around the axis of the last R joint of the RUR chain.

The second leg (or leg 2) has one RU and two identical RUS chains, which can be described as RU/2-RUS. Similarly to leg 1, the first R joint of each chain is mounted on the base with a coaxial configuration. In each chain, the first axis of the U joint is parallel to that of the R joint. The end link of leg 2 is connected to the RU and RUS chains by universal and spherical joints respectively. In consequence, leg 2 can generate three dofs of position by three actuated revolute joints.

For connection with leg 1, the moving platform has two revolute joints orthogonal to each other. In the moving platform's reference frame, an axis of the proximal revolute joint is parallel to the direction of the platform's normal vector. The distal revolute joint is perpendicularly attached to the end link of leg 1. The moving platform has a revolute joint and a spherical joint for connection with leg 2. The axis of the revolute joint is parallel to the normal vector of the moving platform. It is noteworthy that this revolute joint and an attached link, which is referred to as the redundant link, allow the architecture to have a kinematic redundancy. Through an additional dof to the position and orientation dofs of the moving platform, the architecture has seven dofs which is equal to the number of the actuated joints. Therefore, this mechanism has a pure kinematic redundancy without antagonistic forces caused by actuation redundancy.

III. Kinematic Modelling

As shown in Fig. 2(a), a base frame and a moving frame are respectively attached to the base and moving platform, and are noted as $Oxyz$ and $O'x'y'z'$. The reference frames attached to the moving platforms of the end links of leg 1 and leg 2 are denoted as $O'_1x'y'z'$ and $O'_2x'y'z'$ as illustrated in Fig. 2(b) and (c). Vectors $\mathbf{s}_{ij}^k$ and $\mathbf{e}_{ij}^k$ denote the relative joint position vectors and unit vectors of joint axis respectively where i is the order of the chain, j is the order of vector within the chain and k is the number of the leg. $\mathbf{p}$, $\mathbf{Q}_{mp}$, $\boldsymbol{\omega}_{mp}$ and $\mathbf{n}_{mp}$ denote the position, orientation, angular velocity and normal vector of the moving platform respectively. $\mathbf{t}_i$ is the position vector of the proximal revolute joint of the i^{th} leg represented in the frame of the moving platform. $\mathbf{Q}_1$, $\boldsymbol{\omega}_1$, $\mathbf{Q}_2$ and $\boldsymbol{\omega}_2$ are the orientation and angular velocity of end links of leg 1 and leg 2. The vectors in Fig 2(b) and (c) present the position of spherical joints in the moving frame of each end link. Except for the vectors with subscript m and $\mathbf{t}_i$, all vectors are expressed in the base frame.

A. The RUR/3-RUS chains of leg 1

The purpose of the kinematic model of leg 1 is to derive the Jacobian matrices written as

$$\mathbf{J}_1 \begin{bmatrix} \dot{\mathbf{r}}_1 \\ \\ \dot{\theta}_{14}^1 \end{bmatrix} = \mathbf{K}_1 \dot{\boldsymbol{\theta}}^1. \tag{1}$$

$\dot{\boldsymbol{\theta}}^1 = [\dot{\theta}_{11}^1, \dot{\theta}_{21}^1, \dot{\theta}_{31}^1, \dot{\theta}_{41}^1]^T$ is the vector of actuated joint velocities. The Jacobian matrices are readily obtained by considering the kinematics of leg 1. The detailed derivation is omitted here due to space limitations. One obtains

$$\mathbf{J}_1 = \begin{bmatrix} [\mathbf{s}_{34}^1]^T & 0 \\ \mathbf{s}_{23}^{1\,T} + [\mathbf{l}_b \times \mathbf{s}_{23}^1]^T \mathbf{J}_{\omega_1} \mathbf{J}_{r_1}^{-1} & [\mathbf{l}_b \times \mathbf{s}_{23}^1]^T \mathbf{e}_{14}^1 \\ \mathbf{s}_{33}^{1\,T} + [\mathbf{v}_b \times \mathbf{s}_{33}^1]^T \mathbf{J}_{\omega_1} \mathbf{J}_{r_1}^{-1} & [\mathbf{v}_b \times \mathbf{s}_{33}^1]^T \mathbf{e}_{14}^1 \\ \mathbf{s}_{43}^{1\,T} + [\mathbf{w}_b \times \mathbf{s}_{43}^1]^T \mathbf{J}_{\omega_1} \mathbf{J}_{r_1}^{-1} & [\mathbf{w}_b \times \mathbf{s}_{43}^1]^T \mathbf{e}_{14}^1 \end{bmatrix} \tag{2}$$

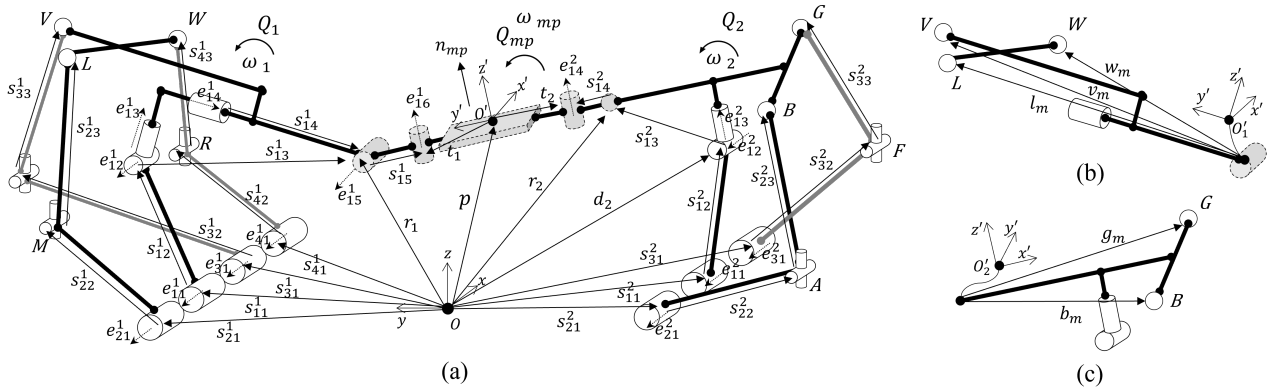

Fig. 2. (a) Description of the proposed robot architecture for fomulating the kinematic model. (b) The end link of leg 1. (c) The end link of leg 2

where $\mathbf{s}^1_{34}$ denotes $\mathbf{s}^1_{13} + \mathbf{s}^1_{14}$ and where $\mathbf{l}_b$, $\mathbf{v}_b$ and $\mathbf{w}_b$ respectively denote $\mathbf{Q}_1\mathbf{l}_m$, $\mathbf{Q}_1\mathbf{v}_m$ and $\mathbf{Q}_1\mathbf{w}_m$. Matrix $\mathbf{K}_1$ is obtained as

$$\mathbf{K}_1 = \begin{bmatrix} {\mathbf{s}^1_{34}}^T\mathbf{u}^1_{11} & 0 & 0 & 0 \\ 0 & {\mathbf{s}^1_{23}}^T\mathbf{u}^1_{21} & 0 & 0 \\ 0 & 0 & {\mathbf{s}^1_{33}}^T\mathbf{u}^1_{31} & 0 \\ 0 & 0 & 0 & {\mathbf{s}^1_{43}}^T\mathbf{u}^1_{41} \end{bmatrix} \quad (3)$$

where $\mathbf{u}^1_{i1}$ denotes $(\mathbf{e}^1_{i1} \times \mathbf{s}^1_{i2})$ and matrices $\mathbf{J}_{r_1}$, $\mathbf{J}_{\omega_1}$ are defined as

$$\mathbf{J}_{r_1} = \begin{bmatrix} (\mathbf{e}^1_{11} \times (\mathbf{s}^1_{12} + \mathbf{s}^1_{13} + \mathbf{s}^1_{14}))^T \\ (\mathbf{e}^1_{12} \times (\mathbf{s}^1_{13} + \mathbf{s}^1_{14}))^T \\ (\mathbf{e}^1_{13} \times (\mathbf{s}^1_{13} + \mathbf{s}^1_{14}))^T \end{bmatrix}^T \quad (4)$$

$$\mathbf{J}_{\omega_1} = \begin{bmatrix} \mathbf{e}^1_{11} & \mathbf{e}^1_{12} & \mathbf{e}^1_{13} \end{bmatrix} \quad (5)$$

The matrix mapping the actuator velocities into the Cartesian velocities can then be written as

$$\mathbf{M}_1 = \mathbf{J}_1^{-1}\mathbf{K}_1. \quad (6)$$

B. The RU/2-RUS chains of leg 2

The Jacobian matrices of leg 2 present the relation between the velocity of $\dot{\mathbf{r}}_2$ and the actuated joint velocities, which can be written as

$$\mathbf{J}_2\dot{\mathbf{r}}_2 = \mathbf{K}_2\dot{\boldsymbol{\theta}}^2. \quad (7)$$

where $\dot{\boldsymbol{\theta}}^2 = [\dot{\theta}^2_{11}, \dot{\theta}^2_{21}, \dot{\theta}^2_{31}]^T$ is the vector of actuated joint coordinates. As mentioned above, matrices $\mathbf{J}_2$ and $\mathbf{K}_2$ are readily obtained and the detailed derivations are omitted. One obtains

$$\mathbf{J}_2 = \begin{bmatrix} {\mathbf{s}^2_{13}}^T \\ {\mathbf{s}^2_{23}}^T + [\mathbf{Q}_2\mathbf{b}_\mathbf{m} \times \mathbf{s}^2_{23}]^T\mathbf{J}_{\omega 2}\mathbf{J}^{-1}_{r_2} \\ {\mathbf{s}^2_{33}}^T + [\mathbf{Q}_2\mathbf{g}_\mathbf{m} \times \mathbf{s}^2_{33}]^T\mathbf{J}_{\omega 3}\mathbf{J}^{-1}_{r_3} \end{bmatrix} \quad (8)$$

$$\mathbf{K}_2 = \begin{bmatrix} {\mathbf{s}^2_{13}}^T\mathbf{u}^2_{11} & 0 & 0 \\ 0 & {\mathbf{s}^2_{23}}^T\mathbf{u}^2_{21} & 0 \\ 0 & 0 & {\mathbf{s}^2_{33}}^T\mathbf{u}^2_{31} \end{bmatrix} \quad (9)$$

where $\mathbf{u}^2_{i1}$ denotes $(\mathbf{e}^2_{i1} \times \mathbf{s}^2_{i2})$. $\mathbf{J}_{r_2}$, $\mathbf{J}_{\omega_2}$ are written as

$$\mathbf{J}_{r_2} = \begin{bmatrix} (\mathbf{e}^2_{11} \times (\mathbf{s}^2_{12} + \mathbf{s}^2_{13}))^T \\ (\mathbf{e}^2_{12} \times \mathbf{s}^2_{13})^T \\ (\mathbf{e}^2_{13} \times \mathbf{s}^2_{13})^T \end{bmatrix}^T \quad (10)$$

$$\mathbf{J}_{\omega_2} = \begin{bmatrix} \mathbf{e}^2_{11} & \mathbf{e}^2_{12} & \mathbf{e}^2_{13} \end{bmatrix} \quad (11)$$

Finally the matrix mapping the joint velocity vectors into vector $\dot{\mathbf{r}}_2$ can be written as

$$\mathbf{M}_2 = \mathbf{J}_2^{-1}\mathbf{K}_2. \quad (12)$$

C. The overall robot architecture

To derive the kinematic model of the robot, four constraint equations related to leg 1 and two constraint equations related to leg 2 are formulated as follows. A first constraint equation on the length of vector $\mathbf{s}^1_{15}$ is written as

$$(\mathbf{p} + \mathbf{Q}_{mp}\mathbf{t}_1 - \mathbf{r}_1)^T(\mathbf{p} + \mathbf{Q}_{mp}\mathbf{t}_1 - \mathbf{r}_1) = |\mathbf{s}^1_{15}|^2. \quad (13)$$

The time derivative of (13) yields

$${\mathbf{s}^1_{15}}^T\dot{\mathbf{p}} + {\mathbf{s}^1_{15}}^T\dot{\mathbf{Q}}_{mp}\mathbf{t}_1 = {\mathbf{s}^1_{15}}^T\dot{\mathbf{r}}_1. \quad (14)$$

The second term on the left side of (14) can be rearranged as

$${\mathbf{s}^1_{15}}^T\dot{\mathbf{Q}}_{mp}\mathbf{t}_1 = (\mathbf{Q}_{mp} \times \mathbf{s}^1_{15})^T\boldsymbol{\omega}_{mp}. \quad (15)$$

By substituting the second term of (14) for (15), (14) can be rewritten as

$${\mathbf{s}^1_{15}}^T\dot{\mathbf{p}} + (\mathbf{Q}_{mp} \times \mathbf{s}^1_{15})^T\boldsymbol{\omega}_{mp} = {\mathbf{s}^1_{15}}^T\dot{\mathbf{r}}_1. \quad (16)$$

The second constraint on the orthogonality of the proximal revolute joint is written as

$$\mathbf{n}^T_{mp}(\mathbf{p} + \mathbf{Q}_{mp}\mathbf{t}_1 - \mathbf{r}_1) = 0. \quad (17)$$

The time derivative of (17) yields

$${\mathbf{s}^1_{15}}^T\dot{\mathbf{n}}_{mp} + \mathbf{n}^T_{mp}\dot{\mathbf{p}} + \mathbf{n}^T_{mp}\dot{\mathbf{Q}}_{mp}\mathbf{t}_1 = \mathbf{n}^T_{mp}\dot{\mathbf{r}}_1. \quad (18)$$

The first term on the left side of (18) can be rewritten as

$${\mathbf{s}^1_{15}}^T\dot{\mathbf{n}}_{mp} = {\mathbf{s}^1_{15}}^T\Omega\mathbf{n}_{mp} = (\mathbf{n}_{mp} \times \mathbf{s}^1_{15})^T\boldsymbol{\omega}_{mp}. \quad (19)$$

The third term on the left side of (18) can be rearranged in the same manner as in (15). Therefore (18) yields

$$\mathbf{n}_{mp}^T\dot{\mathbf{p}} + ((\mathbf{Q}_{mp}t_1 - \mathbf{s}_{15}^1) \times \mathbf{n}_{mp})^T\boldsymbol{\omega}_{mp} = \mathbf{n}_{mp}^T\dot{\mathbf{r}}_1. \quad (20)$$

The third constraint equation of the architecture is the orthogonality between $\mathbf{e}_{15}^1$ and $\mathbf{n}_{mp}$ represented as

$$\mathbf{e}_{15}^{1\,T}\mathbf{n}_{mp} = 0. \quad (21)$$

The time derivative of (21) yields

$$\mathbf{e}_{15}^{1\,T}\dot{\mathbf{n}}_{mp} + \mathbf{n}_{mp}^T\dot{\mathbf{e}}_{15}^1 = 0. \quad (22)$$

Rearranging each term of (22) yields

$$(\mathbf{n}_{mp} \times \mathbf{e}_{15}^1)^T\boldsymbol{\omega}_{mp} = -(\mathbf{e}_{15}^1 \times \mathbf{n}_{mp})^T(\mathbf{J}_{\omega_1}\mathbf{J}_{r_1}^{-1}\dot{\mathbf{r}}_1 + \mathbf{e}_{14}^1\dot{\theta}_{14}^1). \quad (23)$$

The fourth constraint equation on orthogonality between $\mathbf{e}_{15}^1$ and $\mathbf{s}_{15}^1$ can be written as

$$\mathbf{e}_{15}^T(\mathbf{p} + \mathbf{Q}_{mp}\mathbf{t}_1 - \mathbf{r}_1) = 0. \quad (24)$$

The derivative of (24) with respect to the time yields

$$\mathbf{s}_{15}^{1\,T}\dot{\mathbf{e}}_{15}^1 + \mathbf{e}_{15}^T\dot{\mathbf{p}} + \mathbf{e}_{15}^T\dot{\mathbf{Q}}_{mp}\mathbf{t}_1 = \mathbf{e}_{15}^T\dot{\mathbf{r}}_1. \quad (25)$$

Using a similar derivation as in (15), (25) can be rewritten as

$$\mathbf{e}_{15}^T\dot{\mathbf{p}} + (\mathbf{Q}_{mp}\mathbf{t}_1 \times \mathbf{e}_{15}^1)^T\boldsymbol{\omega}_{mp} = \mathbf{e}_{15}^T\dot{\mathbf{r}}_1 + (\mathbf{e}_{15}^1 \times \mathbf{s}_{15}^1)^T\mathbf{J}_{\omega_1}\mathbf{J}_{r_1}^{-1}\dot{\mathbf{r}}_1 - (\mathbf{e}_{15}^1 \times \mathbf{s}_{15}^1)^T\mathbf{e}_{14}^1\dot{\theta}_{14}^1. \quad (26)$$

The fifth and sixth constraint equations on the length of $\mathbf{s}_{14}^2$ and orthogonality of the proximal revolute joint are written as

$$(\mathbf{p} + \mathbf{Q}_{mp}\mathbf{t}_2 - \mathbf{r}_2)^T(\mathbf{p} + \mathbf{Q}_{mp}\mathbf{t}_2 - \mathbf{r}_2) = |\mathbf{s}_{14}^2|^2. \quad (27)$$

$$\mathbf{n}_{mp}^T(\mathbf{p} + \mathbf{Q}_{mp}\mathbf{t}_2 - \mathbf{r}_2) = 0. \quad (28)$$

Similarly to the derivation used in (16) and (20), the time derivative of (27) and (28) yield

$$\mathbf{s}_{14}^{2\,T}\dot{\mathbf{p}} + (\mathbf{Q}_{mp} \times \mathbf{s}_{14}^2)^T\boldsymbol{\omega}_{mp} = \mathbf{s}_{14}^{2\,T}\dot{\mathbf{r}}_2. \quad (29)$$

$$\mathbf{n}_{mp}^T\dot{\mathbf{p}} + ((\mathbf{Q}_{mp}\mathbf{t}_2 - \mathbf{s}_{14}^2) \times \mathbf{n}_{mp})^T\boldsymbol{\omega}_{mp} = \mathbf{n}_{mp}^T\dot{\mathbf{r}}_2. \quad (30)$$

Finally, by combining (16), (20), (23), 26), (29) and (30), the global kinematic model of the robot can be written as

$$\mathbf{J}\mathbf{t} = \mathbf{K}\dot{\boldsymbol{\theta}}. \quad (31)$$

where $\mathbf{t}$ is the vector of Cartesian velocity of the moving platform. The Jacobian matrices of the global architecture have the following form

$$\mathbf{J} = \begin{bmatrix} \mathbf{s}_{15}^{1\,T} & [\mathbf{Q}_{mp}\mathbf{t}_1 \times \mathbf{s}_{15}^1]^T \\ \mathbf{n}_{mp}^T & [(\mathbf{Q}_{mp}\mathbf{t}_1 - \mathbf{s}_{15}^1) \times \mathbf{n}_{mp}]^T \\ \mathbf{0} & [\mathbf{n}_{mp} \times \mathbf{e}_{15}^1]^T \\ \mathbf{e}_{15}^{1\,T} & [\mathbf{Q}_{mp}\mathbf{t}_1 \times \mathbf{e}_{15}^1]^T \\ \mathbf{s}_{14}^{2\,T} & [\mathbf{Q}_{mp}\mathbf{t}_2 \times \mathbf{s}_{14}^2]^T \\ \mathbf{n}_{mp}^T & [(\mathbf{Q}_{mp}\mathbf{t}_2 - \mathbf{s}_{14}^2) \times \mathbf{n}_{mp}]^T \end{bmatrix} \quad (32)$$

$$\mathbf{K} = \begin{bmatrix} \mathbf{s}_{15}^{1\,T} & \mathbf{0} & \mathbf{0} \\ \mathbf{n}_{mp}^T & \mathbf{0} & \mathbf{0} \\ -(\mathbf{e}_{15}^1 \times \mathbf{n}_{mp})^T\mathbf{J}_{M1} & -(\mathbf{e}_{15}^1 \times \mathbf{n}_{mp})^T\mathbf{e}_{14}^1 & \mathbf{0} \\ \mathbf{e}_{15}^{1\,T} - \mathbf{a}_{15}^{1\,T}\mathbf{J}_{M1} & -\mathbf{a}_{15}^{1\,T}\mathbf{e}_{14}^1 & \mathbf{0} \\ \mathbf{0} & \mathbf{0} & \mathbf{s}_{14}^{2\,T} \\ \mathbf{0} & \mathbf{0} & \mathbf{n}_{mp}^T \end{bmatrix} \quad (33)$$

where $\mathbf{a}_{15}^1$ denotes $(\mathbf{e}_{15}^1 \times \mathbf{s}_{15}^1)$ and $\mathbf{J}_{M1}$ is $\mathbf{J}_{\omega_1}\mathbf{J}_{r_1}^{-1}$. The derived Jacobian matrices $\mathbf{J}$ and $\mathbf{K}$ have dimensions 6×6 and 6×7 respectively. The dimension of the matrices reflect the fact that the proposed architecture is kinematically redundant with 7 dofs and 7 actuated revolute joints.

IV. Singularity analysis

Singularities are one of the main reasons for the limited orientational workspace of spatial parallel robots. In particular, singularities critically affect robot performance because the orientational workspace cannot be increased by scaling a robot. In this section, the singularities of leg 1, leg 2 and the moving platform are analyzed separately. In the end, it is shown that the singular configurations of the proposed robot architecture are easily avoided, resulting in a large orientational workspace.

A. Singularity analysis of leg 1 (RUR/3-RUS)

Since leg 1 is a parallel mechanism with four sub-legs, both serial (type I) and parallel (type II) singularities should be investigated. A type I singularity occurs when matrix $\mathbf{K}_1$ in (3) is singular. Since this matrix is a diagonal matrix, the determinant will be zero if any of the diagonal components is zero, leading to a singularity. The component in the first row is zero when $\mathbf{s}_{13}^1+\mathbf{s}_{14}^1$ is orthogonal to $\mathbf{e}_{11}^1$ or $\mathbf{s}_{13}^1+\mathbf{s}_{14}^1$ is colinear with $\mathbf{s}_{12}^1$. The other diagonal components are zero if the first link $\mathbf{s}_{i2}^1$ and second link $\mathbf{s}_{i3}^1$ are colinear or $\mathbf{s}_{i2}^1 \times \mathbf{s}_{i3}^1$ is orthogonal to $\mathbf{e}_{i1}^1$ where i indicates 2, 3, and 4. Such configurations causing the singularities occur when the leg is at the edge of its workspace. For example, increasing the roll angle of the leg stretches the side sub-leg resulting in decreasing the angle between the first link and second link of the side leg. Therefore, these singularities can be avoided by sacrificing the workspace at or near the boundary and by proper dimensioning of the links.

A type II singularity of leg 1 occurs when matrix $\mathbf{J}_1$ in (2) is singular. Because of the complexity of the matrix, the singularity was analyzed by calculating the condition number at a representative workspace numerically. Since all first revolute joints of the different chains are mounted coaxially, the workspace has an axial symmetric torus shape with respect to the axis of the first joints. Therefore, the workspace on the $\mathbf{XY}$ plane including the axis of the first joint was selected without losing the validity of the analysis. In addition, an area where x is positive was considered due to the symmetry of the robot. Because θ_{14}^1 cannot be expressed by the end position of leg 1, 0, $\pi/6$ and $\pi/3$ were selected as representative angles. Fig. 3(a) presents the condition number in the workspace of leg 1 when θ_{14}^1 is 0. It was

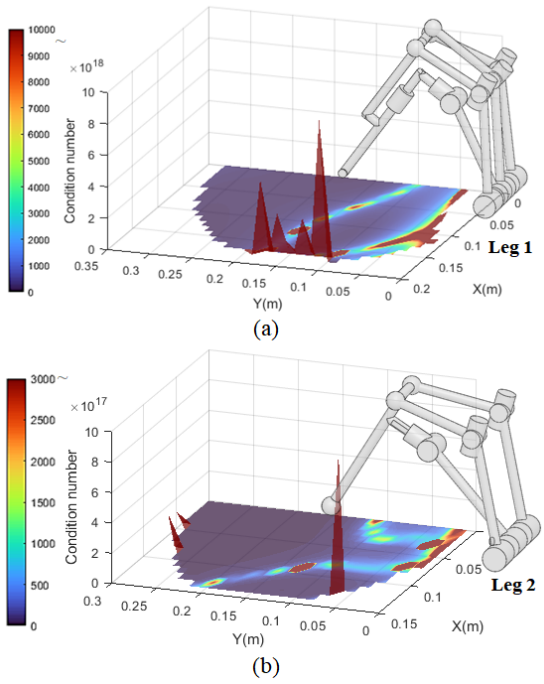

Fig. 3. Results of type II singularity analysis by calculating the condition number. (a) The condition number of leg 1 when θ_{14}^1 is zero. (b) The condition number of leg 2

observed that, regardless of the changes in angle θ_{14}^1, type II singularities occur at the edge of the workspace in the x-axis direction. Also, the area adjacent to the leg's base yields large values of the condition number. However, because these areas are placed at the edge of the workspace, these singularities can be easily handled by the same approach applied to the type I singularities. Relatively large condition numbers were observed inside the workspace in configurations that vary according to the value of θ_{14}^1. Although these condition numbers could worsen the dynamic performance of the robot, it is not a critical flaw of the proposed architecture.

B. Singularity analysis of leg 2 (RU/2-RUS)

The type I singularity of leg 2 occurs if $\mathbf{K}_2$ in (9) is singular. Since $\mathbf{K}_2$ is a diagonal matrix, each element should not be zero to avoid the singular condition. These components are zero if $\mathbf{s}_{i2}^2$ and $\mathbf{s}_{i3}^2$ are colinear or $(\mathbf{s}_{i2}^2 \times \mathbf{s}_{i3}^2)$ is orthogonal to $\mathbf{e}_{i1}^2$, where the i indicates 1, 2, and 3. The method applied for leg 1 was used for the type II singularity of leg 2. As shown in Fig. 3(b), this singularity occurs at the edge of the workspace. Consequently, the singularities of leg 2 can be easily avoided using the same approaches used for leg 1.

C. Singularity analysis considering the configuration of the moving platform

The parallel singularity that has a fatal impact on the orientational workspace of the parallel mechanism was analyzed using a geometrical approach. This singularity occurs when the determinant of the matrix in (32) is zero. Each row of the

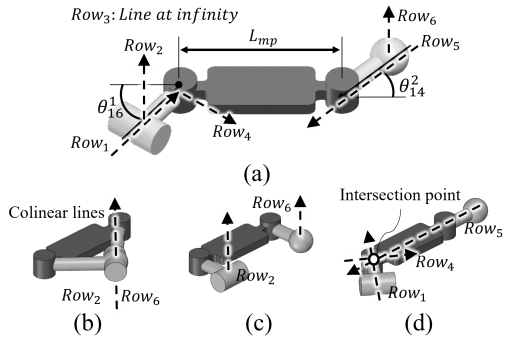

Fig. 4. (a) The description of the moving platform. Row_i illustrates the Plücker line corresponding to i^{th} row vector of $\mathbf{J}$ (b) The first singularity case of the group1 matrix. (c) The second singularity case of the group1 matrix. (d) The singularity case of the group2

$\mathbf{J}$ matrix can be expressed as a line by Plücker coordinates. In the row vector, the first three components determine the direction of the line, and the last three components indicate a position where the line passes. Fig. 4(a) illustrates the Plücker lines of the Jacobian matrix $\mathbf{J}$. The third-row vector cannot be visualized in Fig. 4 (a), because it is a line at infinity. Geometrical conditions of these Plücker lines can determine the singularity of the matrix by introducing the Grassmann line geometry (GLG). The six Plücker lines are divided into two groups and expressed in the moving frame to simplify the analysis, yielding

$$\mathbf{J}_{group1} = \begin{bmatrix} 0 & 0 & 1 & d_2 & e_2 & 0 \\ 0 & 0 & 0 & d_3 & e_3 & 0 \\ 0 & 0 & 1 & d_6 & e_6 & 0 \end{bmatrix} \tag{34}$$

$$\mathbf{J}_{group2} = \begin{bmatrix} a_1 & b_1 & 0 & 0 & 0 & f_1 \\ a_4 & b_4 & 0 & 0 & 0 & f_4 \\ a_5 & b_5 & 0 & 0 & 0 & f_5 \end{bmatrix} \tag{35}$$

where the subscripts denote a corresponding row number. The first group consists of the second, third and sixth row vectors and the remaining vectors form the second group. These two groups are linearly independent because linear combinations of one group cannot generate the vectors belonging to the row space of the other group. According to the GLG, the divided Jacobian matrix will lose its rank when the three Plücker lines intersect at one point or are parallel to each other on a plane.

In case of group 1, there are two conditions of the singularity. The one condition is that the Plücker lines corresponding to the first and third row of $\mathbf{J}_{group1}$ are colinear, as shown in Fig. 4(b). This singularity can be avoided by a restriction on the link length as $|\mathbf{s}_{15}^1| + |\mathbf{s}_{14}^2| < L_{mp}$. As illustrated in Fig. 4(c), the other condition occurs when θ_{14}^2 and θ_{15}^1 are $\pi/2$ and $-\pi/2$, respectively. If the restriction of $|\mathbf{s}_{15}^1| \neq |\mathbf{s}_{14}^2|$ is imposed on the link length, this singularity can also be avoided. In short, proper dimensioning of the moving platform can avoid the singularities of the first group.

For group 2, the lines of the first row and second row in $\mathbf{J}_{group2}$ are always orthogonal to each other. Therefore, the

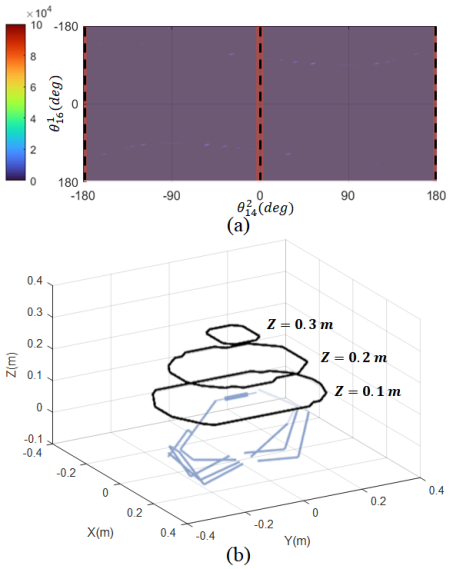

Fig. 5. (a) A Result of the type II singularity analysis considering the configuration of the moving platform. The dash line represents a position where the condition number is infinity. (b) A constant orientation workspace.

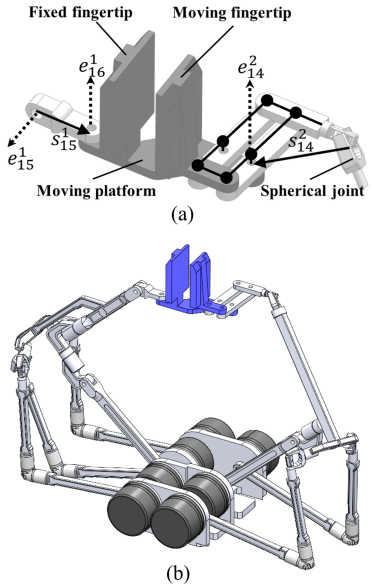

Fig. 6. (a) Gripping mechanism. (b) A CAD model of the 6+1-dof hybrid parallel robot.

$\mathbf{J}_{group2}$ will be singular when angle θ_{14}^2 is zero so that three lines have an intersection point, as shown in Fig. 4(d). Here, the advantages of kinematic redundancy are emphasized that allow changing angle θ_{14}^2 while maintaining the position and orientation of the moving platform. The singularity of group 2 is completely avoided using the redundant leg. As shown in Fig. 5(a), the singularity analysis of $\mathbf{J}$ in (32) using a numerical approach also led to the same results. The parallel singularity occurs only when θ_{14}^2 is 0 or π independently from θ_{16}^1, so the redundant leg has a singularity free angular operating range. This operating range is exploited further to generate a gripping function. Fig. 5(b) illustrates the constant orientation workspace of the robot architecture.

V. Gripping Mechanism Operated by the Redundant Leg

As shown in Fig. 6(a), the gripping mechanism utilizes a parallelogram to transform the rotation of the redundant leg into the translation of a gripper jaw. The spherical joint at the end of leg 2 is connected to one of the parallelogram links which rotate around the $\mathbf{e}_{14}^2$ axis. The moving gripper jaw is mounted on a certain link of the parallelogram. The other jaw is fixed to the moving platform. As a result, the rotation of the redundant leg can generate the translational motion of the moving jaw and change the distance between the jaw to achieve a gripping motion. It is noteworthy that the redundant dof is effectively utilized not only to avoid the singularity but also to generate the grip function.

VI. Virtual Prototype and Video Animations

A CAD model of the prototype is presented in Fig. 6(b). Direct drive actuators were chosen to achieve high backdrivability. The animation of the virtual prototype is provided as supplemental material for this article. The animation consists of three parts. At first, the translational motion of the robot is demonstrated based on straight paths. The second part shows the variation of the moving platform's orientation, including the rotation around axes of the global coordinates. The last part presents the gripping motion generated remotely by the actuators mounted on the base.

VII. Conclusion

In this article, a novel (6+1)-dof kinematically redundant hybrid parallel robot was introduced. Compared to the previous architecture suggested in [21], the number of redundant dof and legs was reduced. In addition, the novel parallel legs with 3 and 4 dofs were proposed to minimize the moving inertia by mounting actuators on the base. The serial and parallel singularity analysis of each leg showed that singularities can be easily avoided by proper dimensioning of the robot and by sacrificing the edge of the workspace. The parallel singularity analysis of the robot architecture was conducted based on a geometrical approach. As a result, the proposed architecture can avoid this singularity by controlling the redundant leg resulting in a large orientational workspace. Moreover, the redundant leg was further exploited to generate gripping motion. The gripping function without an additional actuator at the moving platform also helps to decrease the moving inertia. Owing to the use of direct drive motors in the prototype design, the robot can achieve high backdrivabilty and low impedance. Due to the advantages mentioned above, it is expected that the robot will be well suited for delicate pERI tasks. Current work includes the optimization of the robot dimensions considering the dynamic properties of the robot, the optimization of the gripper mechanism and the development of a prototype.

REFERENCES

[1] G. J. Monkman, S. Hesse, R. Steinmann, and H. Schunk, *Robot Grippers*. John Wiley and Sons, 2007.

[2] T. Laliberté and C. M. Gosselin, "Simulation and design of underactuated mechanical hands," *Mechanism and Machine Theory*, vol. 33, no. 1, pp. 39–57, 1998.

[3] G. A. Kragten, M. Baril, C. Gosselin, and J. L. Herder, "Stable precision grasps by underactuated grippers," *IEEE Transactions on Robotics*, vol. 27, no. 6, pp. 1056–1066, 2011.

[4] A. Bhatia, A. M. Johnson, and M. T. Mason, "Direct drive hands: Force-motion transparency in gripper design," *Robotics: science and systems*. [Online]. Available: https://par.nsf.gov/biblio/10105126

[5] N. C. Dafle, A. Rodriguez, R. Paolini, B. Tang, S. S. Srinivasa, M. Erdmann, M. T. Mason, I. Lundberg, H. Staab, and T. Fuhlbrigge, "Extrinsic dexterity: In-hand manipulation with external forces," in *2014 IEEE International Conference on Robotics and Automation (ICRA)*. IEEE, 2014, pp. 1578–1585.

[6] S. Yuan, A. D. Epps, J. B. Nowak, and J. K. Salisbury, "Design of a roller-based dexterous hand for object grasping and within-hand manipulation," in *2020 IEEE International Conference on Robotics and Automation (ICRA)*. IEEE, 2020, pp. 8870–8876.

[7] S. Yuan, L. Shao, C. L. Yako, A. Gruebele, and J. K. Salisbury, "Design and control of roller grasper v2 for in-hand manipulation," in *2020 IEEE/RSJ International Conference on Intelligent Robots and Systems (IROS)*. IEEE, 2020, pp. 9151–9158.

[8] A. J. Spiers, B. Calli, and A. M. Dollar, "Variable-friction finger surfaces to enable within-hand manipulation via gripping and sliding," *IEEE Robotics and Automation Letters*, vol. 3, no. 4, pp. 4116–4123, 2018.

[9] C. M. McCann and A. M. Dollar, "Design of a stewart platform-inspired dexterous hand for 6-dof within-hand manipulation," in *2017 IEEE/RSJ International Conference on Intelligent Robots and Systems (IROS)*. IEEE, 2017, pp. 1158–1163.

[10] V. V. Patel and A. M. Dollar, "Robot hand based on a spherical parallel mechanism for within-hand rotations about a fixed point," in *2021 IEEE/RSJ International Conference on Intelligent Robots and Systems (IROS)*. IEEE, 2021, pp. 709–716.

[11] F. Ostyn, B. Vanderborght, and G. Crevecoeur, "Design and control of a quasi-direct drive robotic gripper for collision tolerant picking at high speed," *IEEE Robotics and Automation Letters*, vol. 7, no. 3, pp. 7692–7699, 2022.

[12] A. Bhatia, A. M. Johnson, and M. T. Mason, "Direct drive hands: Force-motion transparency in gripper design," in *Robotics: science and systems*, 2019.

[13] S. Tanaka, K. Koyama, T. Senoo, M. Shimojo, and M. Ishikawa, "High-speed hitting grasping with magripper, a highly backdrivable gripper using magnetic gear and plastic deformation control," in *2020 IEEE/RSJ International Conference on Intelligent Robots and Systems (IROS)*. IEEE, 2020, pp. 9137–9143.

[14] Y. Karako, S. Kawakami, K. Koyama, M. Shimojo, T. Senoo, and M. Ishikawa, "High-speed ring insertion by dynamic observable contact hand," in *2019 International Conference on Robotics and Automation (ICRA)*. IEEE, 2019, pp. 2744–2750.

[15] I. Ebrahimi, J. A. Carretero, and R. Boudreau, "3-prrr redundant planar parallel manipulator: Inverse displacement, workspace and singularity analyses," *Mechanism and Machine Theory*, vol. 42, no. 8, pp. 1007–1016, 2007.

[16] ——, "A family of kinematically redundant planar parallel manipulators," *Journal of Mechanical Design*, vol. 130, no. 6, 2008.

[17] C. Gosselin and L.-T. Schreiber, "Kinematically redundant spatial parallel mechanisms for singularity avoidance and large orientational workspace," *IEEE Transactions on Robotics*, vol. 32, no. 2, pp. 286–300, 2016.

[18] J. Lacombe and C. Gosselin, "Singularity analysis of a kinematically redundant (6+ 2)-dof parallel mechanism for general configurations," *Mechanism and Machine Theory*, vol. 176, p. 105015, 2022.

[19] C. Gosselin, T. Laliberté, and A. Veillette, "Singularity-free kinematically redundant planar parallel mechanisms with unlimited rotational capability," *IEEE Transactions on Robotics*, vol. 31, no. 2, pp. 457–467, 2015.

[20] K. Wen, D. Harton, T. Laliberté, and C. Gosselin, "Kinematically redundant (6+ 3)-dof hybrid parallel robot with large orientational workspace and remotely operated gripper," in *2019 International Conference on Robotics and Automation (ICRA)*. IEEE, 2019, pp. 1672–1678.

[21] K. Wen, T. S. Nguyen, D. Harton, T. Laliberté, and C. Gosselin, "A backdrivable kinematically redundant (6+ 3)-degree-of-freedom hybrid parallel robot for intuitive sensorless physical human–robot interaction," *IEEE Transactions on Robotics*, vol. 37, no. 4, pp. 1222–1238, 2020.